A Survey of the Polarized Emission from the Galactic Plane at 1420 MHz with Arcminute Angular Resolution

T.L. Landecker[1], W. Reich[2], R.I. Reid[1,3], P. Reich[2], M. Wolleben[1,2], R. Kothes[1,4], B. Uyanıker[1,5], A.D. Gray[1], D. Del Rizzo[1], E. Fürst[2], A.R. Taylor[4], and R. Wielebinski[2]

[1] National Research Council of Canada, Herzberg Institute of Astrophysics, Dominion Radio Astrophysical Observatory, P.O. Box 248, Penticton, British Columbia, V2A 6J9, Canada

[2] Max-Planck-Institut für Radioastronomie, Auf dem Hügel 69, 53121 Bonn, Germany

[3] Present address: National Radio Astronomy Observatory, 520 Edgemont Road, Charlottesville, Virginia 22903-2475, USA

[4] Department of Physics and Astronomy, University of Calgary, 2500 University Drive N.W., Calgary, AB, Canada

[5] Present address: 35/3737 Gellatly Road, Westbank, British Columbia, V2T 2W8, Canada

ABSTRACT

Context. Observations of polarized emission are a significant source of information on the magnetic field that pervades the Interstellar Medium of the Galaxy. Despite the acknowledged importance of magnetic field in interstellar processes, our knowledge of field configurations on all scales is seriously limited.

Aims. This paper describes an extensive survey of polarized Galactic emission at 1.4 GHz that provides data with arcminute resolution and complete coverage of all structures from the broadest angular scales to the resolution limit, giving information on the magneto-ionic medium over a wide range of interstellar environments.

Methods. Data from the DRAO Synthesis Telescope, the Effelsberg 100-m Telescope, and the DRAO 26-m Telescope have been combined. Angular resolution is ~1′ and the survey extends from $\ell = 66°$ to $\ell = 175°$ over a range $-3° < b < 5°$ along the northern Galactic plane, with a high-latitude extension from $\ell = 101°$ to $\ell = 116°$ up to $b = 17°.5$. This is the first extensive polarization survey to present aperture-synthesis data combined with data from single antennas, and the techniques developed to achieve this combination are described.

Results. The appearance of the extended polarized emission at 1.4 GHz is dominated by Faraday rotation along the propagation path, and the diffuse polarized sky bears little resemblance to the total-intensity sky. There is extensive depolarization, arising from vector averaging on long lines of sight, from H II regions, and from diffuse ionized gas seen in Hα images. Preliminary interpretation is presented of selected polarization features on scales from parsecs (the planetary nebula Sh 2-216) to hundreds of parsecs (a superbubble GSH 166−01−17), to kiloparsecs (polarized emission in the direction of Cygnus X).

Key words. Polarization – Techniques: polarimetric – Surveys – Galaxy: disk – ISM: magnetic fields – H II regions

1. Introduction

The detection of linear polarization in the Galactic radio emission (Westerhout et al. 1962; Wielebinski et al. 1962) provided crucial evidence in establishing the synchrotron mechanism as the source of the emission. Assumption of equipartition between relativistic particles and magnetic field then led to estimates of the field strength of a few μG (Beck 2001), and the best estimates today do not differ substantially (Sun et al. 2008). The magnetic field in the Galaxy is a significant reservoir of energy, and the field is likely to play an important role in interstellar processes. Nevertheless, more than four decades after the first detection our knowledge of the field configuration on global and local scales is still quite limited.

The apparent promise of polarization observations has proved difficult to translate into hard information on field configurations. First, the observed fractional polarization is generally far below the 70% theoretical maximum. The radiation is optically thin and superposition of emission contributions along the line of sight can "depolarize" the signal through vector averaging. Second, Faraday rotation operates whenever the signal propagates through a magnetized thermal plasma. Emission and Faraday rotation often occur in the same region, and a wide variety of depolarization effects occur (Burn 1966; Sokoloff et al. 1998). Furthermore, a typical radio telescope operating at low radio frequencies proves to be more sensitive to the Faraday rotation of a plasma region than to its bremsstrahlung (as discussed in Section 8.3). The net result of all these effects is that the polarized sky rarely resembles the total-intensity sky and interpretation of polarization images is seldom simple.

Angular resolution of early polarization surveys with single antennas was poor. A comprehensive set of surveys of the northern sky was published by Brouw & Spoelstra (1976) based on well calibrated (but undersampled) observations at four frequencies between 408 MHz and 1411 MHz made in the 1960s with

the Dwingeloo 25-m Telescope; angular resolution ranged from 2° to 36′. Here the subject rested for many years until it was revived using the Effelsberg 100-m Telescope in the late 1980s. Extensive surveys made with that telescope had resolutions of 4.′3 at 2695 MHz (Junkes et al. 1987; Duncan et al. 1999) and 9.′4 at 1410 MHz (Uyanıker et al. 1998, 1999; Reich et al. 2004). A wide-area survey of the Southern Galactic plane was made with the Parkes Telescope at 2417 MHz with resolution 10.′4 (Duncan et al. 1997). The Northern Galactic plane was surveyed with the Urumqi Telescope with resolution 9.′5 at 4900 MHz (Sun et al. 2007; Gao et al. 2010). The WMAP data at 23 GHz and higher frequencies (Hinshaw et al. 2009) cover the entire sky at an angular resolution smaller than 1° and, on simple lines of sight, show almost the intrinsic polarization characteristics because Faraday rotation at these frequencies is extremely low.

A substantial increase in angular resolution has been provided by aperture-synthesis telescopes, and observations of the Galactic polarized emission with angular resolutions from one to a few arcminutes have been made in recent years (Wieringa et al. 1993; Gray et al. 1998, 1999; Haverkorn et al. 2000; Gaensler et al. 2001; Uyanıker & Landecker 2002; Uyanıker et al. 2003; Haverkorn et al. 2003a,b,c, 2006). These observations have revealed much about Faraday rotation in the ISM, but interpretation has been hampered by the lack of information on the biggest structures[1].

An interferometer observes the sky through a spatial high-pass filter, so the zero levels for Q and U are lost. Both polarized intensity, PI $= \sqrt{Q^2 + U^2}$, and polarization angle, PA $= 0.5 \tan^{-1}\left(\frac{U}{Q}\right)$, change in a very non-linear fashion in response to errors in zero levels. The most serious effect is on angle. Consider an observation of a region several tens of beamwidths in extent comprising broad structure, whose polarization angle, A, varies only slowly across the area, and fine structure, contributing rapid changes in PA that add vectorially to A. An interferometer can measure only the rapid angle changes, and, if the broad structure is not measured, the apparent PA will vary over a large range, whereas the true distribution of angle is much narrower and is centred on A. Examples of this effect are illustrated in Reich (2006), Sun et al. (2007), and Gao et al. (2010). An example in the present data is discussed in Section 8.6. If broad structure is missing then conclusions about PA, and hence rotation measure (RM), are prone to serious error. In contrast, the work described here is the first extensive polarization survey to incorporate single-antenna data with aperture-synthesis data.

In this paper we present a survey of the polarized emission at 1420 MHz covering 1060 square degrees of the northern Galactic plane with an angular resolution of ~1 arcminute. With 1.5×10^7 independent data points this is the largest polarization survey published to date. The survey combines data from the DRAO Synthesis Telescope, the Effelsberg 100-m Telescope, and the DRAO 26-m Telescope, and we discuss the techniques that we have developed to combine these datasets. Data from two single-antenna telescopes, not just one, were needed to correctly represent broad structure for reasons discussed below (Section 4.2).

The new polarization dataset forms part of the Canadian Galactic Plane Survey (the CGPS, described by Taylor et al. 2003). The scientific goal of the CGPS is the study of the Galactic "ecosystem", the interplay between the various constituents of the ISM, their role in star formation, the impact of stars on their environments, and the interaction of Galaxy-wide

Table 1. DRAO Synthesis Telescope survey characteristics

Coverage	$66° < \ell < 175°, -3° < b < 5°$; $101° < \ell < 116°, 5.0° < b < 17.°5$
Individual field size	107.′2 diameter to 50% 150.′0 diameter to 25.7%
Field used in mosaicking	150′ diameter
Field centre spacing	112′ on triangular grid
Observation dates	1995.3 to 2004.4
Survey area	1060 square degrees
Observing rate	150 square degrees per year
Bandwidth	30 MHz in four bands of 7.5 MHz each
Centre frequencies	1407.2, 1414.1, 1427.7, and 1434.6 MHz
Angular resolution	$58'' \times 58''$ cosec δ
System temperature	60 K, 1995.3 to 2003.4; 45 K, 2003.4 to 2004.4
Sensitivity (mosaicked data)	0.30 mJy/beam rms 1995.3 to 2003.4 76 sin (declination) mK; 0.23 mJy/beam rms 2003.4 to 2004.4 58 sin (declination) mK

phenomena such as density waves with ISM constituents. The CGPS comprises surveys[2] of the atomic hydrogen (the 21-cm H i line), the ionized gas (seen in radio continuum), the molecular gas (the lines of CO near 115 GHz - (Heyer et al. 1998)), the dust (IRAS data reprocessed with high resolution - (Cao et al. 1997; Kerton & Martin 2000)), and, relevant here, the relativistic component and the magnetic field traced by continuum observations at 408 MHz (total intensity only) and 1420 MHz (Stokes parameters I, Q, and U). The survey described here maps the magneto-ionic component of the ISM with unprecedented detail and precision.

2. Telescopes and signal processing equipment

2.1. The DRAO Synthesis Telescope

A detailed description of the DRAO Synthesis Telescope can be found in Landecker et al. (2000); only an outline is given here, with emphasis on changes since that paper was published and on polarization properties. Telescope characteristics relevant to this survey are summarized in Table 1.

The telescope consists of seven antennas, of diameter ~9 m. The antennas receive right-hand and left-hand circular polarization (RHCP and LHCP) at 1420 MHz; the maximum baseline of 617 m gives an angular resolution of ~1′ at that frequency. A telescope attribute that strongly influences polarimetry is the slight difference in construction of the seven antennas. Two antennas have diameter $d = 9.14$ m and focal length $f = 3.81$ m ($f/d = 0.42$) while the remainder have $d = 8.53$ m and focal length $f = 3.66$ m ($f/d = 0.43$). The symmetrical reflectors have prime-focus feeds supported by struts whose construction differs slightly on the various antennas. These seemingly minor differences have a considerable effect on polarization properties and special procedures have been developed to correct images of polarized emission for instrumental polarization (see Section 3.5).

---

[1] Single-antenna data may also suffer from this problem – see Section 4.2 and Reich (2006)

[2] The CGPS database is accessible to the astronomy community at `http://www3.cadc-ccda.hia-iha.nrc-cnrc.gc.ca/cgps/`

For continuum imaging at 1420 MHz the telescope has four frequency bands, each of width $\Delta f = 7.5$ MHz, two below and two above the frequency of the H I line. In operation the telescope is tuned to the H I centre frequency; because of changes in the relative velocity of telescope and source the centre frequency changes (for example due to the Earth's rotation and orbital motion). The image formation algorithms use the exact centre frequency at which a data sample was observed (different for each band). For the CGPS observations the central velocity to which the receiver is tuned varies from $v_{lsr} = -40$ km s^{-1} at $\ell = 66°$ to $v_{lsr} = -60$ km s^{-1} at $\ell = 175°$. This variation corresponds to a frequency change of about 90 kHz, 1.3% of the width of an individual band and an inconsequential fraction of the centre frequency. The nominal centres of the four continuum bands lie at ±6.25 MHz and ±13.75 MHz from the central tuning frequency but small bandshape errors mean that the effective centre frequencies deviate slightly from these values. The deviations have been measured and are taken into account; the effective centre frequencies for the four bands are listed in Table 1. Velocity corrected effective centre frequencies are preserved in data headers and are used, for example, in calculations of RM.

The DRAO Synthesis Telescope is characterized by good sensitivity to extended structure and a very thorough sampling of the u-v plane. The shortest baseline is 12.9 m, 61 wavelengths at 1420 MHz, nominally giving the telescope sensitivity to structures at least as large as ~40′. The u-v sampling interval is $L = 4.29$ m, about half the antenna diameter. Consequently, the first grating response is at an angular radius where the antenna response is very low and grating responses to objects within the field of view lie well outside the field.

2.2. The Effelsberg 100-m Telescope

The Effelsberg 100-m telescope (Hachenberg et al. 1973) is a fully steerable high precision antenna with surface deviations of about 0.5 mm (rms) that is based on the concept of homologous elevation-dependent deformations. L-band observations are always made from the prime focus. In this frequency band elevation-dependent gain variations can be ignored.

A detailed measurement of the antenna pattern at λ21 cm was made by Kalberla et al. (1980). A feed with a slightly different taper was used later, when Uyanıker et al. (1998) measured an area of $1°1 \times 1°1$ around 3C 123 covering the main beam and the first and second sidelobes. The shape of the main beam can be very well approximated by a circular Gaussian with a HPBW of 9′35. Sidelobes are enhanced in the direction of the four subreflector support struts and the first sidelobes have peak responses of about −20 dB. The conversion between main beam brightness temperatures T_B and Jy/beam area is 2.12 K/Jy. The L-band receiving system has two channels with cooled HEMT amplifiers for LHCP and RHCP covering 1.29 to 1.72 GHz, and has a system noise of about 26 K. Because of interference the frequency band for continuum observations has to be close to 1.4 GHz with a typical bandwidth of 20 MHz, avoiding Galactic H I emission. An IF correlation polarimeter provides two total power channels and two correlated channels proportional to Stokes U and Q. Further details of the receiving system are given by Uyanıker et al. (1998). In 2001 a second IF-polarimeter was added allowing simultaneous observations with centre frequencies at 1395 MHz and 1408 MHz and a bandwidth of 14 MHz each. A new IF polarimeter was installed in 2002, offering eight 4-MHz channels, normally centred at 1402 MHz. Telescope characteristics relevant to this survey are summarized in Table 2.

Table 2. Effelsberg 100-m Telescope survey characteristics

Coverage	$25° < \ell < 230°$,
	$-20° < b < 20°$;
Observation dates	1994 to 2005
Bandwidth (B)[1]	20 MHz
Frequency (F)[1]	1400 MHz
Angular resolution	9′35
System temperature	26 K
Sensitivity (rms noise U,Q)	8 mK

[1] Occasional interference required decreases in B, which never fell below 10 MHz, and/or increases in F, which never rose above 1410 MHz.

Table 3. DRAO 26-m Telescope survey characteristics

Coverage	Right Ascension: 0^h to 24^h,
	Declination: $-29°$ to $90°$
Observation dates	2002.9 to 2003.5 and 2004.5 to 2005.3
Bandwidth	12 MHz
Frequency	1410 MHz
Angular resolution	36′0
System temperature	125 K
Sensitivity (rms noise U,Q)	12 mK

2.3. The DRAO 26-m Telescope

The DRAO 26-Telescope is an equatorially mounted, axially symmetric reflector. At 1.4 GHz the aperture efficiency is ~53%. Pointing accuracy is ~1′. Data for the present work were drawn from the survey of Wolleben et al. (2006) and the telescope and receiver are described in full in that paper; relevant telescope characteristics are summarized in Table 3.

The two hands of circular polarization were generated from linear outputs of the prime-focus feed using a coaxial quadrature hybrid. The beamwidth was 36′ at 1.4 GHz. The receiver was uncooled, and yielded a system temperature of ~125 K. The RHCP and LHCP outputs were processed in an IF analog polarimeter, of the type used for the Effelsberg observations, which generated all polarization products.

3. Observation and processing of Synthesis Telescope data

3.1. Observations

The DRAO Synthesis Telescope has only seven antennas but samples the u-v plane thoroughly using multiple array configurations; as a consequence the mapping speed is slow, only 150 square degrees per year. The observation period for the present survey was long, from 1995 April to 2004 March. Observations were made day and night, although solar interference and increased Faraday rotation in the ionosphere make daytime less than ideal for polarimetry. Unavoidably, over the long period, some telescope parameters changed, but, on the positive side, image processing techniques were improved. The observations began just before a minimum of solar activity (at ~1996.5), through a maximum at ~2001, and well into a second minimum, with the attendant changes in ionospheric conditions. For all these reasons the data product is less uniform than one observed over a shorter time span.

Full details of the observation technique for the CGPS can be found in Taylor et al. (2003). Details relevant to the polarization survey can be found in Table 1. The latitude coverage of the survey, $-3° < b < 5°$, was biased north of the nominal Galactic plane because of the warp of the northern Galactic disk.

3.2. Calibration

The telescope was calibrated using small-diameter extragalactic sources, with preference given to 3C 147 and 3C 295, known to be unpolarized, but 3C 48 was also used (Smegal et al. 1997). Observations were interspersed with calibrations, usually at intervals of 12 hours. Assumed flux densities are consistent with the scale of Baars et al. (1977) – see Landecker et al. (2000) for details. After calibration the correlator outputs are known in units of flux density; this applies to polarization outputs as well as total-intensity outputs. The PI calibration of the survey is therefore tied to the well established flux density scale. PA was calibrated from observations of the polarized source 3C 286, made at intervals of four days (Taylor et al. 2003).

3.3. Image processing

Image formation generally followed the conventional practices of aperture-synthesis technique; processing specific to the CGPS is described in Taylor et al. (2003). The modified CLEAN algorithm developed by Steer et al. (1984) works well on images with extended structure and was used exclusively. The usual next step, self-calibration, is ineffective on polarization images because they contain very little flux. Because antenna phase and amplitude gains are the same for all cross-correlations, gain solutions derived from self-calibration of RHCP and LHCP total-intensity images could be applied to the cross-hand products that were used to make polarization images.

After these initial procedures some artefacts remained in the images, centred on bright sources inside and outside the primary beam. Because of the wide field of view and small differences between the individual antennas of the array, complex gain errors occur at large distances from the field centre. The resulting artefacts affect I data but are more pronounced in Q and U images because the instrumental polarization rises rapidly with distance from the field centre (see Section 3.5). The artefacts are not easily removable by standard self-calibration techniques because the assumption of uniform complex gains over the primary beam is incorrect. They are removed by the procedure called MODCAL (Willis 1999) which is, in principle, a position-dependent self calibration.

Initially this procedure was used for strong sources as close as $40'$ from the field centre. Later in the progress of the survey the instrumental polarization correction described in Section 3.5 was applied and artefacts around strong sources were reduced to the point where use of MODCAL was seldom required.

3.4. Solar and terrestrial interference and emission from the ground

The antenna sidelobes are highly polarized and sources outside the primary beam can produce strong spurious polarized signals even if their emission is not inherently polarized. The Sun is such a source: it traverses the antenna sidelobes whenever it is above the horizon, contributing ~1 K to antenna temperature. Conversion of I to Q or U can be as high as 50% in the far side-lobes (Ng et al. 2005) so the Sun can contribute a polarized sig-

nal up to 500 mK. However, because of the Sun's large extent its effects are usually confined to shorter baselines. Spurious solar signals were removed to a satisfactory level by making images centred on the Sun's position and removing the response from the visibilities. Use of MODCAL to adjust phases in the direction of the Sun improved the removal process.

Terrestrial interference, which is always polarized, is another source of spurious polarization. Interference may come from any direction, but, because the telescope is an east-west interferometer, persistent terrestrial interference appears in images as rings centred at the north celestial pole. Making a $640'$ wide image of the north polar cap and subtracting its Fourier transform from the visibilities proved to be an effective way of removing it. Again, MODCAL improved the removal.

Radiation from the ground appears as polarized emission because of the conversion of I into Q and U by the sidelobes. A patch of ground can radiate the same signal into two adjacent antennas when they are close together, producing a strong correlated signal in polarization channels. This effect is more difficult to remove, and polarization data gathered at the shortest baseline (~12.9 m) were mostly unusable for polarization imaging (while being quite usable for imaging of I and H i). Data from the Effelsberg Telescope were used to provide these spatial frequencies for polarization imaging.

When a reasonably good image can be formed of an interfering source, subtracting its Fourier transform from the visibilities is much better than completely removing ("flagging") the affected data, but there is inevitably some confusion with real structure on the sky at those spatial frequencies. However, in some particularly bad cases the data for affected interferometer spacings were simply flagged and removed.

3.5. Correction for instrumental polarization

Two levels of correction for instrumental polarization were required. The feed and associated waveguide components do not provide perfect LHCP and RHCP and there is coupling between the two polarized outputs. The regular telescope calibration (see Section 3.2) corrected for these effects, which apply to the whole field of view. The calibration technique is described in Smegal et al. (1997). After this calibration the spurious polarization at field centre was nominally zero with an accuracy estimated to be 0.25% of I.

Beyond this correction it is also necessary to correct for instrumental polarization that varies with position across the field of view. These effects result in the conversion of I into Q, U, and V. In other words, sources which are unpolarized appear to be polarized, and sources which are partially polarized appear in images with altered polarization properties. Spurious polarized features appear mainly wherever there is a strong point source or a strong unpolarized extended source such as an H ii region.

Two investigations have been made of this effect. The effect has been studied by Ng et al. (2005) using electromagnetic analysis software. Instrumental polarization depends on the polarization performance of the feeds, on reflector curvature, and on aperture blockage by the feed-support struts, among other more minor effects such as surface roughness. Because the antennas are equatorially mounted the instrumental polarization response remains fixed on the field of view throughout an observation and it is possible to make an image-based correction.

The image-based correction for instrumental polarization was derived from observations of an unpolarized source at a grid of positions across the main beam. Details, and images of the instrument response, may be found in Taylor et al. (2003). The

correction was a *scalar* correction: at any position in the field, spurious Q and U were calculated as a fraction of I at that point, and the correction function was determined for the aggregate of the seven antennas. Spurious Q and U so derived were simply subtracted from measured Q and U. Individual corrections for the four frequency bands were determined and were applied separately.

Subsequently, a more sophisticated correction technique was developed by Reid et al. (2008) and used for 60% of the survey data. The reflector-induced instrumental polarization is not purely a scalar quantity: it has phase as well as amplitude. Furthermore, it is quite strongly dependent on the details of antenna construction; the calculations of Ng et al. (2005) show this quite clearly. The ultimate correction must take into account the complex nature of this response, and to enable us to do so we made a further set of observations of the effect. Once again, an unpolarized source was observed at a grid of positions across the antenna main beam. These measurements were made in a holographic mode: the reference source (in this case 3C 295) was placed at the centre of the field of view of one antenna and the other antennas were moved. Complex visibilities were measured at 15′ increments across the beam of each antenna.

The data resulting from these holographic measurements were used in the image formation process. For each CLEAN component obtained from processing the I image, spurious Q and U visibilities were computed using the measured properties of the antennas participating in each baseline. The sum of these over all CLEAN components was then subtracted from Q and U visibilities, and Q and U images were computed from the modified visibilities.

At large angular distances from the pointing centre the conversions of energy between the Stokes parameters increase and the primary beams are less well known. Therefore, when making a mosaic of polarization images the data for any one field were not used beyond a radius of 75′. In contrast, for total-intensity imaging the equivalent radius is 90′.

4. Observation and processing of the Effelsberg 100-m data

4.1. Observations

Polarization data from the Effelsberg 100-m telescope are part of the *Effelsberg Medium Latitude Survey* (EMLS: Reich et al. 2004). Survey characteristics are given in Table 2.

Observations were made only at night to avoid spurious contributions from the Sun seen in the telescope sidelobes. The extended observation time needed for accurate determination of zero level and the contribution of ground radiation was not available, and the survey area was divided into subfields of typical size $10° \times 10°$ with $5°$ as the smallest and $16°$ as the longest scan length. Individual subfields were treated as separate observations. Each subfield was observed at least twice in orthogonal directions in Galactic co-ordinates with a scanning speed of $4°$/min, giving a total integration time for each 4′ pixel of 2 sec.

4.2. Data processing

A linear baseline was removed from each scan, setting I, Q, and U to zero at the ends; this effectively removed ground radiation from the observations but also filtered off the largest structure. Scans were calibrated against the noise source, and spiky interference was excised. Scanning effects were suppressed using the method of unsharp masking (Sofue & Reich 1979). Following

Junkes et al. (1987), the means of Q and U for each scan were assumed to be zero. Orthogonal scans were then reconciled using the "plait" algorithm (Emerson & Gräve 1988). By assembling plaited maps for the entire survey area we avoided edge effects at the boundaries between subfields. Accurate observations of I, Q, and U then depend on data from smaller telescopes to provide the zero level and large-structure information. For I observations the Stockert data (Reich 1982; Reich & Reich 1986) provided the missing information. For Q and U observations Uyanıker et al. (1998) made initial attempts to use the data of Brouw & Spoelstra (1976). When this proved inadequate because of the sparse sampling of that dataset, an initiative was launched to provide the necessary data from the DRAO 26-m telescope, ultimately leading to the survey of Wolleben et al. (2006). That survey is used here.

The Effelsberg total-intensity data are confusion limited at a level of 15 mK T_B or about 7 mJy/beam area. The polarization channels Q and U are less affected by confusion and have a typical rms noise level of 8 mK T_B. Instrumental polarization was reduced to a residual level of less than 1% by the technique described by Uyanıker et al. (1998).

5. Observation and processing of the DRAO 26-m data

The data for the present work were drawn from the absolutely calibrated survey of the polarized emission from the northern sky at 1410 MHz made by Wolleben et al. (2006). Details can be found in that paper, and only a few facts about the survey are repeated here.

Observations were made as drift scans, with the telescope stationary on the meridian; observations were made only at night to avoid the effects of the Sun in the telescope sidelobes. Data were fully sampled along the scans, but the separation between scans was generally larger than required for full sampling with a 36′ beam. Averaged over the survey region (spanning declination $-29°$ to $+90°$), coverage was 42% of full Nyquist (half-beamwidth) sampling.

The telescope accepts both circular polarizations, and Stokes parameters Q and U were derived from the complex product of LHCP and RHCP generated in an analog correlator. Measurements of total intensity were made from detectors in a separate signal path: I and PI therefore required separate calibration.

The standard polarization calibrator (3C 286) was used to calibrate the Effelsberg observations, but could not be used for the 26-m survey. Its polarized flux density, of the order of 1.5 Jy at 1.4 GHz, generates only ~140 mK in the 36′ beam, small compared to the polarized signal from the Galactic emission on which the source is superimposed, and comparable to variations in that background. Tying the survey to the work of Brouw & Spoelstra (1976) at 946 points across the sky provided the required calibration of the polarization products.

The final rms noise level of the 26-m data was 12 mK in Q and U. Systematic errors were estimated to be less than 50 mK.

6. Intercomparison of calibration of the three surveys

Three quite disparate datasets must be combined to form the final images and it is important to know that the three calibrations are consistent. The calibration of the DRAO 26-m data (Wolleben et al. 2006) is tied to the data of Brouw & Spoelstra (1976). The

calibration of the Effelsberg 100-m data is based on the assumed polarized flux density of 3C 286 and a conversion of flux density to brightness temperature (Uyanıker et al. 1998). The calibration of the DRAO Synthesis Telescope is based on assumed flux densities for 3C 147 and 3C 295, both unpolarized sources, for PI, and on 3C 286 for PA (see Section 3.2). In this Section we investigate the consistency of these three calibrations.

6.1. Comparison of the 26-m and 100-m scales

The calibration of the DRAO 26-m survey is tied to the Dwingeloo survey, itself calibrated using an assumed flux density for Cas A and a measured value of antenna gain (Brouw & Spoelstra 1976). Wolleben et al. (2006) compared the DRAO 26-m and Effelsberg scales over two regions 1200 and 640 square degrees in area. The Effelsberg data were smoothed to 36′, the resolution of the 26-m Telescope. Scans across the smoothed data in right ascension were derived, and compared with actual scans made with the DRAO 26-m Telescope. The two sets of scans were not directly comparable because of the suppression of large-scale features in the Effelsberg data, but it was assumed that the missing data could be approximated by polynomials. The coefficients of these polynomials, of orders 1 to 3, and a scaling factor for the 26-m data were derived by a fitting procedure. The derived scaling factor was 0.94, indicating that the scale of Brouw & Spoelstra (1976) was 6% too high. The origin of this discrepancy is not clear, but it appears to be within the errors of the Dwingeloo survey, especially taking into account subsequent refinements of the flux density scale (Baars et al. 1977; Ott et al. 1994).

We have compared the two datasets in a different way, using data from a region of area 726 square degrees. Images from both datasets were prepared including only structure between 36′ and 2° in size. Great care was taken to eliminate edge effects by starting with data from larger regions before any spatial filtering was attempted. Q and U images were processed independently. Filtered images from the two datasets closely resemble each other. A pixel-by pixel comparison is shown in Fig. 1. Regression lines fitted to these data do not have a slope of exactly 1.0 and do not pass exactly through the point (0,0). We cannot explain this small effect and have therefore not used regression analysis, but have simply taken the ratio of all the data points shown. This ratio is 0.96±0.01 (26-m/100-m). We conclude that the two intensity scales are within ~5%.

6.2. Comparison of the 100-m and Synthesis Telescope scales

The PI and PA scales of the Effelsberg 100-m Telescope and the DRAO Synthesis Telescope are likely to be very close. The 100-m Telescope is calibrated using 3C 286 for total intensity and PI. The Synthesis Telescope is calibrated using 3C 147 and 3C 295. Both telescopes rely on the same authority for the flux densities of these sources, the work of Baars et al. (1977) and Ott et al. (1994). Furthermore, the 15-year experience of combining Effelsberg and DRAO data during the entire time span of the CGPS indicates that the alignment between the intensity scales is within a few percent.

Nevertheless, a comparison of PI and PA scales was undertaken to allay any concern about scale errors and to check our analysis methods. The two telescopes have a generous overlap in the u-v plane, but polarized regions are not strong emitters, so the comparison was limited by sensitivity. The region cho-

sen for the comparison was an area $4° \times 4°$ centred on $\ell = 98°$, $b = 1°$ observed by both telescopes. This region contains bright polarized emission displaying structure on both large and small scales, and the images contain significant spectral power at the spatial frequencies where both telescopes have significant sampling.

The data in the $4° \times 4°$ region were placed in a larger image and tapered smoothly to zero at the edges. The larger image was Fourier transformed to the visibility domain. The extension avoided the artefacts that are introduced when transforming data with abrupt discontinuities; the exact nature of the tapering function (a cubic polynomial was used) did not have a strong effect on the outcome of the comparison. The transformed 100-m data were then corrected for the angular resolution of the telescope (9′.35) by dividing the visibilities by the transform of the beam (approximated as a Gaussian function reaching half power at 35 m, approximately one third of the antenna diameter). The equivalent process (dividing by the transform of the synthesized beam) was applied to the Synthesis Telescope data. For each dataset, an approximate power spectrum was constructed by averaging the power in the visibility plane in rings. The same processing was applied independently to Q and U images.

Fig. 2 shows the results. At baselines below 15 m the power in the 100-m data exceeds that from the Synthesis Telescope. This is as expected because the interferometer cannot sample structure on those scales. In the range 5 to 15 m the 100-m data provides the better representation of the emission structure. At the very shortest baselines, not shown in Fig. 2, the power spectrum of the Effelsberg data drops again, a consequence of setting values to zero at the edge of each observation subfield. At high spatial frequencies the corrected 100-m power spectrum exhibits a strong rise, attributable to the amplification of noise and high-frequency scanning artefacts that results from dividing the visibilities by a function whose value is rapidly approaching zero. A single antenna obtains a noisy estimate of the image power at its resolution limit: the finest details in an image made with a single antenna are measured with very low weight.

Inspection of Fig. 2 shows that the two datasets are in good agreement over the baseline range from about 15 m to 70 m. The ratio (100-m to Synthesis Telescope) is very close to unity at 55 m and averages 1.15 ± 0.2 in the range 15 to 50 m where both datasets are used. The uncertainty was estimated from careful consideration of the main source of error, our limited knowledge of the beamshapes. As noted above, both sets of visibilities have been divided by the transform of the beam. For the Effelsberg data this process boosts visibilities at 35 m by a factor of 2 and by larger factors at larger baselines. The Effelsberg beam has been approximated by a Gaussian which matches the observed beam well within the half-power beamwidth, but does not fit the lower levels well and has a different solid angle than the actual beam. The Synthesis Telescope beam varies slightly from place to place because of data loss and other factors, but the effect on the comparison is smaller. Considering these facts, and the noise level of the data, as well as our initial confidence in the calibration reliability, we made no further scale corrections in combining the data from the 100-m Telescope and the Synthesis Telescope. There is no systematic imbalance between the Q and U ratios, implying that the PA scales for the two telescopes agree. We conclude that the scales of the two datasets are probably within 10%.
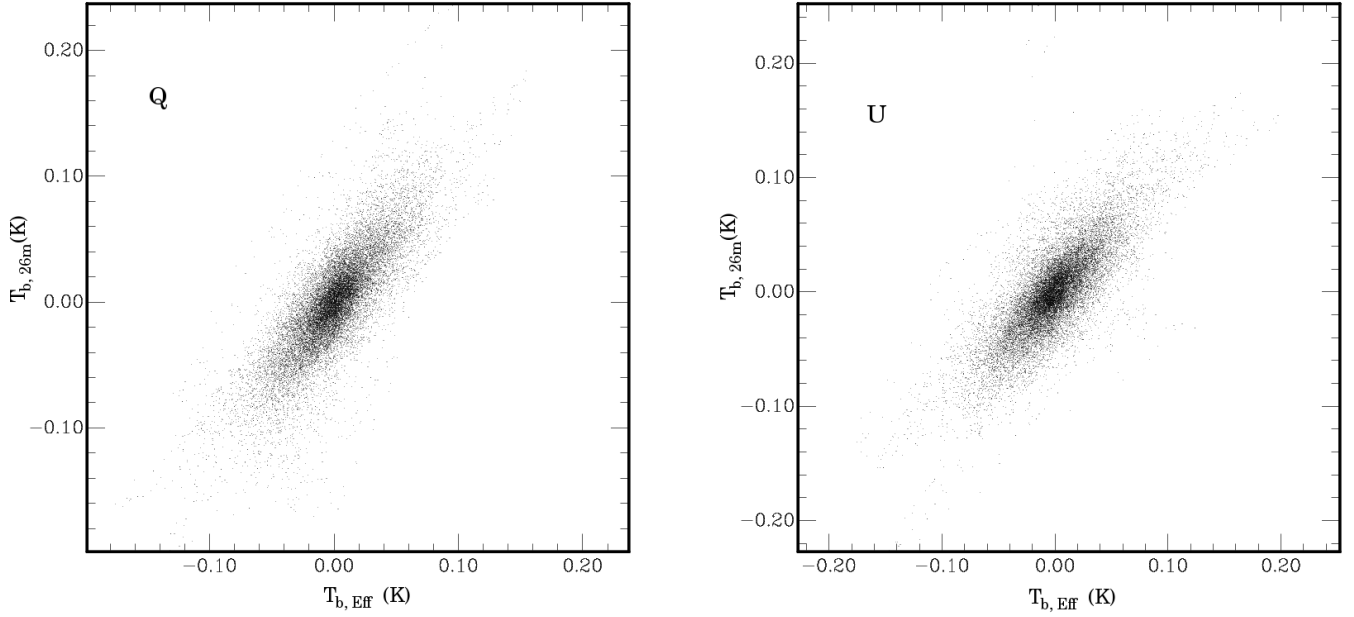
Fig. 1. Point-by-point comparison of brightness temperature values in images derived from Effelsberg 100-m data (x-axis) and DRAO 26-m data (y-axis) over an area of 726 square degrees. Axis scales are linear. Data have been filtered to include only structure of size between 36′ and 2°. Q data are shown in the left panel and U data in the right. See text for details.
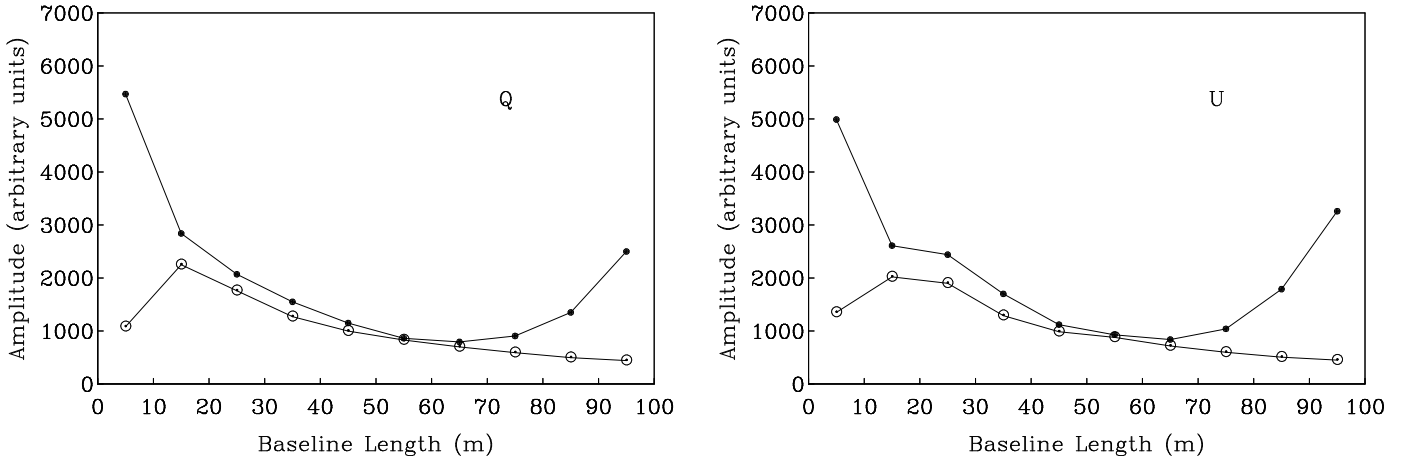
Fig. 2. Power spectra of polarization data in a region of size $4° \times 4°$ centred at $\ell = 98°$, $b = 1°$ for Q (left panel) and U (right panel) derived from data obtained with the Effelsberg 100-m Telescope (filled circles) and the DRAO Synthesis Telescope (open circles). See text for details.

7. Combining the three datasets

Data from all three telescopes are needed to create a high-fidelity, high-resolution image of the polarized sky. The 26-m Telescope provides measurements with correct zero levels, but has poor resolution. The Effelsberg data have better resolution but lack information on structures larger than a few degrees because of the manner in which data were taken and ground radiation removed. The Synthesis Telescope has good angular resolution but information corresponding to broad structures cannot be sampled by the interferometer. The combination process applies the appropriate spatial filtering to account for the transfer functions of the individual telescopes.

Fourier-transform techniques are regularly used to combine single-antenna and aperture-synthesis data in the CGPS (see Taylor et al. 2003 for details). However, the 26-m polarization dataset presents the problem of undersampling. One choice

is to use the interpolated image (as described by Wolleben et al. 2006) but after combination with the Effelsberg data artefacts remained that were obviously related to the undersampling. Fourier-transform techniques were ruled out, but we set out to devise a process that exploited the information content of each dataset to the maximum extent possible.

The first step was to improve the interpolation across the gaps in the 26-m data. In place of linear or other mathematical interpolation, we used information from the Effelsberg 100-m data. We smoothed the Effelsberg data to 36′. We worked in Galactic co-ordinates, processing data along lines of constant longitude, one longitude at a time. Where 26-m data points were available we used them. Across a gap where no 26-m data were available, we used smoothed Effelsberg data, "lifting" the data to attach it smoothly to the 26-m data points at each end. This process did not fill the gaps perfectly, but obviously brought in more
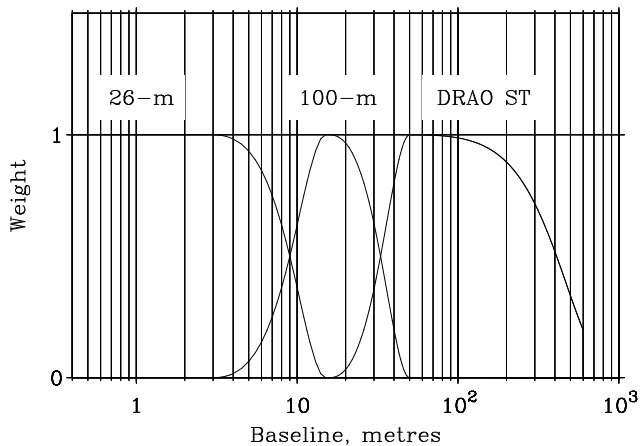
Fig. 3. Approximate spatial filtering applied in the combination of datasets from the DRAO 26-m Telescope, the Effelsberg 100-m Telescope, and the DRAO Synthesis Telescope. Because image-domain methods were used to combine the 26-m and 100-m datasets (see text) the filter functions that overlap at 9 m, although approximately correct, are notional.

information about the sky than a simple linear interpolation. The result of this step (which we refer to as the final 26-m image) was our best estimate of the sky seen with a 26-m telescope. We then had a dataset which sampled structure with a filtering function whose half-power level was at about 9 metres, or 45 wavelengths (see Fig. 3). This dataset was then combined with the Effelsberg 100-m dataset using a process described by Reich et al. (1990). The Effelsberg data were smoothed to the resolution of the final 26-m image, and the difference computed. The difference represents structure that is not present in the original Effelsberg image (the broad structure filtered off by the observing technique), and this was then added to the Effelsberg data. The result of this step is to restore the broad structure that is removed in the Effeleberg data reduction procedure.

Fig. 3 shows the weighting functions used in the combination in a diagrammatic fashion. The process that we used to combine 26-m and Effelsberg data on average blended the data between baselines 3 m and 15 m (3 m, about 15 wavelengths, corresponds to an angular size of 4°, the smallest area mapped in the Effelsberg survey). The ideal weighting function is at 0.5 at 9 m, matching closely the weighting of the 26-m beam. Fourier transform methods were used to combine the [26-m + 100-m] dataset with the Synthesis Telecope data over the range of 15 to 50 m. The weighting function for single-antenna data is at 0.5 at ~33 m, again very close to the weighting of the 100-m beam. Also shown in Fig. 3 is the Gaussian apodization function, reaching 20% at the longest baseline (617 m), that has been applied to the Synthesis Telescope data.

7.1. Spurious Features and Error estimates

Some spurious features remain in the images, originating in all three datasets. Some image defects in the Synthesis Telescope data (ring structures) can be seen around the position of Cas A (G111.7−2.1). Similar rings can be seen around the position of the H ɪɪ region W3 (G133.7−1.2). Cas A could not be imaged with adequate dynamic range by the Synthesis Telescope and an area around it was set to zero in that dataset. Sidelobe responses are also very evident in the Effelsberg data around Cas A.

Residual instrumental polarization in the Effelsberg data is less than 1% (Reich et al. 2004). Residual errors in instrumental polarization for an individual field from the Synthesis Telescope are estimated at 0.25% for the field centre, growing to 1% at a distance of 75′. Instrumental polarization over the vast majority of the area presented here is below 0.5%. These estimates are based both on the expected accuracy of the measurements for the correction, and the observed discrepancies between overlapping fields. Noise on Synthesis Telescope data was 0.30 mJy/beam rms in mosaicked images for the earlier part of the survey and 0.23 mJy/beam in the later stages, corresponding to 76 and 58 sin (declination) mK respectively (see Table 1).

Our investigation (Section 6) of the relative calibration of the three datasets has led to the conclusion that (a) the discrepancy between the 26-m and 100-m scales is less than 5%, and (b) the discrepancy between the 100-m scale and the aperture-synthesis scale is less than 10%. An unknown error remains in the single-antenna data as a result of the undersampling present in the 26-m Telescope data.

The noise on the 26-m Telescope data is 12 mK rms and systematic errors are ≤50 mK (Wolleben et al. 2006). These errors transfer to the final data presented here. Polarized intensity images presented in this paper have not been corrected for noise bias.

The three datasets were observed at slightly different centre frequencies and with different bandwidths, possibly leading to incorrect results. We considered four sources of error, differing bandwidth depolarization, systematic differences in polarization angle at different frequencies, intrinsic variations in polarized intensity with frequency, and variations in polarization angle of calibration sources.

For a value of |RM| = 100 rad m^{-2}, the highest value observed in a Rotation Measure synthesis study of the Northern sky by Wolleben et al. (2010), the bandwidth depolarization in the four bands of the Synthesis Telescope averaged together is about 0.15%. Bandwidths used with the Effelsberg 100-m and DRAO 26-m Telscopes are smaller, and bandwidth depolarization is correspondingly less. For the same values of RM, the angle rotation between the different centre frequencies has a maximum value of ~7.5°. The RM of the great bulk of emission is far less than 100 rad m^{-2}, probably less than 20 rad m^{-2}, making these errors negligible in comparison to other effects.

Assuming a temperature spectral index of 2.7 for synchrotron emission at our frequency, the 20 MHz spread in centre frequencies makes a difference of ~4% between amplitude scales. This may explain some of the ratio of ~1.15 found between Effelsberg 100-m and DRAO Synthesis Telescope scales (Section 6.2) but the uncertainties are high and we have not made any adjustment to the intensity scales. The flux densities used for the different amplitude calibrators were appropriate for the operating frequencies of the individual telescopes and no errors arise from the difference in observing frequencies beyond the effect of spectral index variation of the emission itself. The primary calibrator of polarization angle, 3C286, has almost zero RM, making its polarization angle nearly independent of frequency.

8. Results

This section presents the results of the survey with some preliminary interpretation. The data presented in this paper, together with data for other significant ISM constituents, are available at http://www3.cadc-ccda.hia-iha.nrc-cnrc.gc.ca/cgps/. Details of the data format may be found in Taylor et al. (2003).
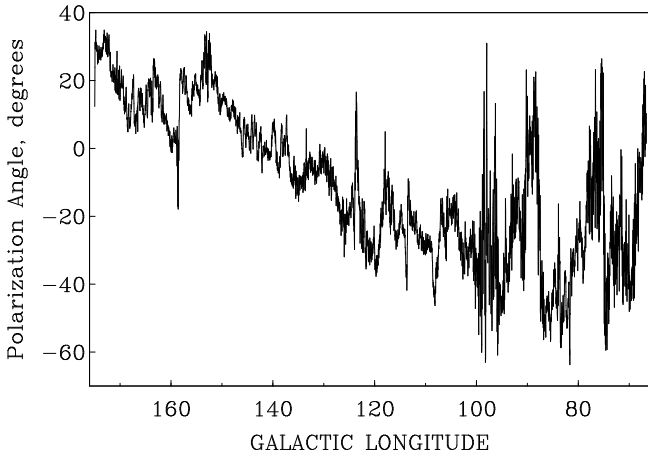
Fig. 8. A representative plot showing variation of polarization angle averaged over a strip 20′ wide centred on $b = 1°$.

8.1. The images

Figure 4 shows the major part of the survey, along the Galactic plane, using a representation that shows both PI and PA. Figs. 5, 6 and 7 present I and PI for the same area. Each panel covers 20° of longitude, with an overlap of 2° between figures. Figure 9 presents the data for the high-latitude extension, again showing PI and PA. The survey data are shown at full angular resolution.

We are presenting the largest survey yet of the polarized emission from the Milky Way and the first extensive survey to combine single-antenna data with aperture-synthesis data. We expect new results from such an advance, and indeed we have discovered a number of surprising phenomena. Here we attempt no more than a broad-brush interpretation, emphasizing major themes that appear to be new while paying relatively little attention to particular objects. Future papers will deal with many different results from this survey.

Over the region covered by our data the diffuse polarized sky bears little resemblance to the total-intensity sky. A similar remark has been made about virtually every polarization survey undertaken at decimetre wavelengths throughout the history of the subject. The widely accepted interpretation is that the polarized features we detect are largely the product of Faraday rotation and do not reflect structure in the Galactic synchrotron emission. The exceptions are supernova remnants (SNRs) and pulsar-wind nebulae and, in particular, the North Polar Spur, seen at high positive latitudes, *e.g.* Wolleben et al. (2006); Wolleben (2007) (and not covered in our survey), and "point" sources, mostly extragalactic. SNRs are discussed in Section 8.4. Point source RMs are discussed in detail by Brown & Taylor (2001) and Brown et al. (2003) and will not be considered here.

An origin in Faraday rotation means automatically that polarized "objects" will usually not look like things seen in other wavebands. The polarized sky is almost entirely "new", and the first problem we should tackle is taxonomy, a classification of polarization features. We will not attempt that in any thorough way here, but our choice of the small number of features that we do describe may point the way for a future study.

8.2. Large-scale features

We begin with a description of some of the large-scale features of the data seen in Fig. 4. There is a gradual increase in PI and a fairly smooth change of PA of about 70° with in-

creasing longitude. The angle variation is illustrated in Fig. 8. The Cygnus region obviously ceates a major disturbance in the range $65° < \ell < 100°$ but the large-scale trend is nevertheless clear. These trends were already evident in the DRAO 26-m data (Wolleben et al. 2006), and are preserved at high angular resolution. The large-scale changes are probably connected with the large-scale features of the magnetic field, roughly aligned with the spiral structure, while the small-scale polarization structures reflect the irregular component and the turbulence of the ionized gas (field is probably tied to electron density to some extent). At our observing frequency of 1.4 GHz, the irregular component does not seem to dominate the regular one, at least for $\ell \gtrsim 110°$. At longer wavelengths, where Faraday rotation is larger, the small-scale fluctuations may eventually overwhelm the large-scale variation.

Such systematic changes over a large fraction of the Galactic disk imply that the large-scale magnetic field affects the diffuse Galactic emission, either through the emission process or through depolarization mechanisms. The RMs of extragalactic compact sources seen through this part of the disk have also been shown to change in a systematic fashion (Brown & Taylor 2001; Brown et al. 2003). The regular component of the local magnetic field is directed towards $\ell \approx 85°$ (Noutsos 2009). Along lines of sight close to this direction Faraday rotation will be high and a number of depolarization mechanisms will be active (*e.g.* Sokoloff et al. 1998). As the line of sight moves towards the anticentre it gradually becomes perpendicular to the regular component of the magnetic field and Faraday rotation will decrease. Synchrotron emission is lower in this part of the Galaxy as shown by lower total-intensity levels, but depolarization effects apparently drop off even more rapidly, with the net result that PI rises and polarization fraction increases. The reduced amount of interstellar matter towards the edge of the Galaxy will also significantly lower depolarization.

The angle gradient seen in Fig. 8 is consistent in sense with the change in RM of extragalactic sources seen in Brown & Taylor (2001) and Brown et al. (2003) but the change in angle of ~70° between $\ell \approx 100°$ and $\ell \approx 180°$ is less by a factor of about 8 than the rotation implied by the change in RM over the same range, a change of ~200 rad m^{-2}. The data of Wolleben et al. (2006) reveal strong depolarization along this section of the Galactic plane, so we are not seeing all of the polarized emission. The large-scale emission, which dominates the polarization angle, is probably mostly local emission (see discussion of depolarization in Section 8.3).

8.3. Small-scale structure and depolarization

Chaotic structure, apparently uncorrelated with any other ISM tracer, has been the hallmark of high-resolution polarization images since they were first made (see the references in the Introduction to this paper). The present survey fits this pattern. Our results (Figs. 5, 6, and 7) show that small-scale structure is seen almost everywhere in our data.

Faraday rotation that varies with position can break large, smooth emission features into smaller polarization structures. Faraday rotation in a turbulent medium will therefore affect the power spectrum of the polarized sky, moving power from broad structure to smaller scales. At 1420 MHz this process must be active to some extent, but large-scale features are still detectable and indeed are dominant, as noted in Section 8.2. Faraday rotation depends on wavelength squared and there is undoubtedly some wavelength at which the large-scale structure has virtually disappeared from polarization data.
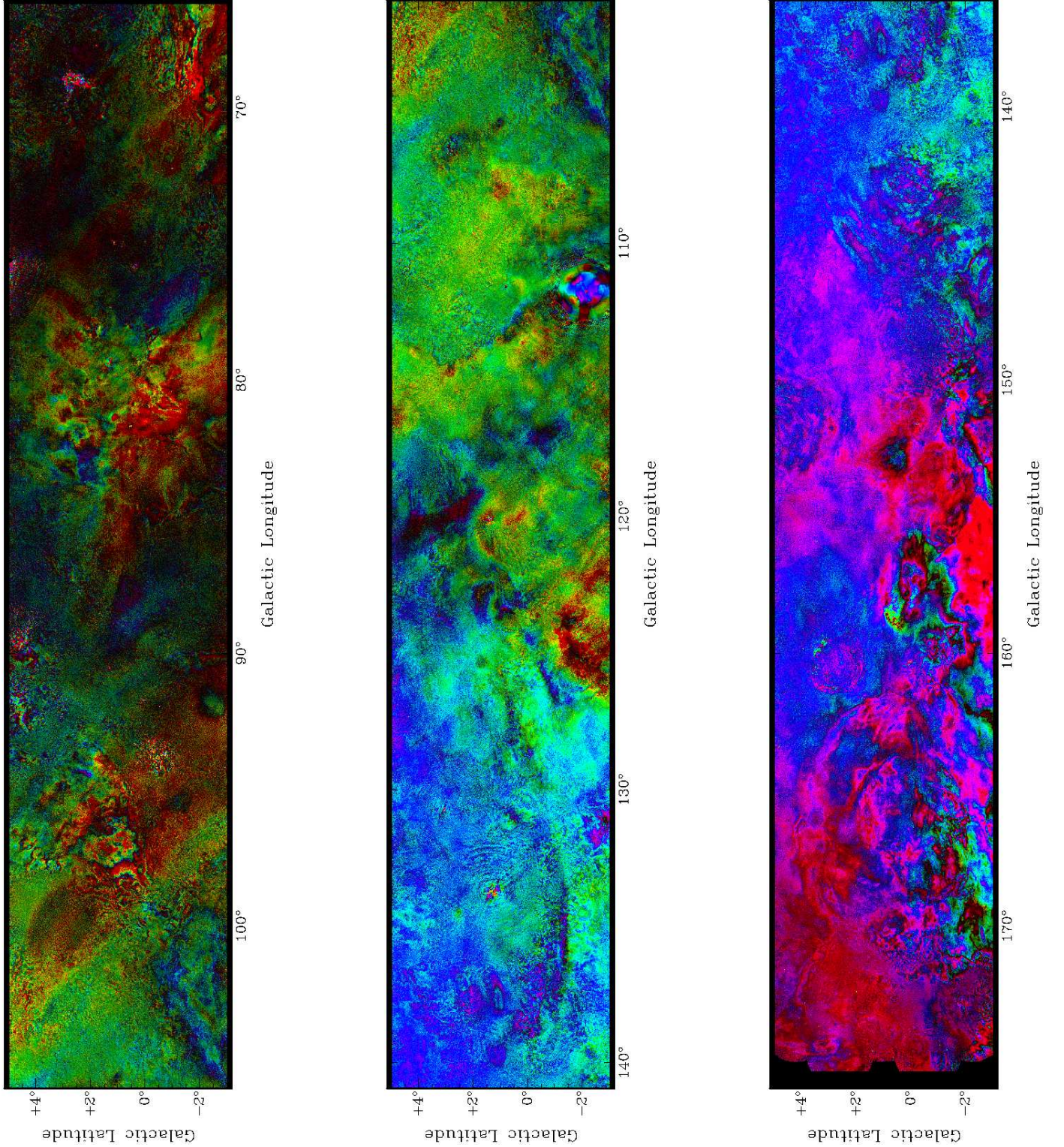
Fig. 4. Polarization data along the Galactic Plane. In this representation intensity of colour depicts polarized intensity and hue depicts polarization angle. The range of polarized intensity is zero (dark) to 0.45 K (bright). The range of polarization angle is from $-50°$ to $+30°$, chosen because most values of angle in the region lie in this range. Regions near $\ell = 65°$ have PA$\approx-50°$ and are shown in red. Angle changes smoothly through orange, yellow, green, blue, and purple, to red again near $\ell = 175°$ where PA$\approx+30°$.

As noted in the introduction, radio telescopes at decimetre wavelengths are often more sensitive to the Faraday rotation produced by ionized gas than to its total-intensity emission. For example, consider an ionized region of extent 10 pc with electron density 0.5 cm^{-3} in a magnetic field with line-of-sight compo-

nent 2 μG. At 1420 MHz this region will produce a Faraday rotation of 20°, which is easily detectable with the DRAO Synthesis Telescope. The same H II region produces an emission measure of 2.5 cm^{-6} pc, one tenth the thermal noise in the I image. For the Effelsberg 100-m Telescope the angle change will be the same,
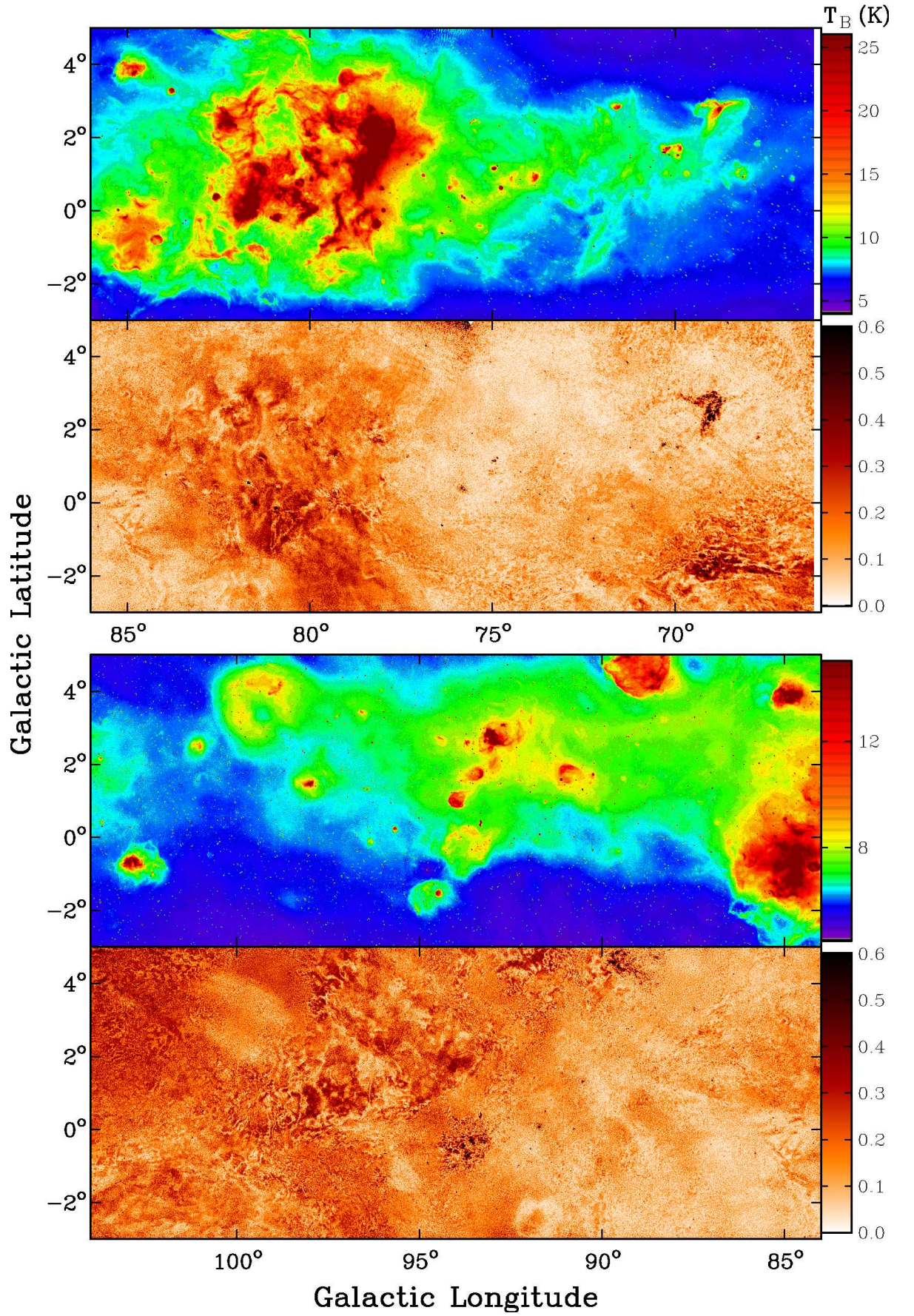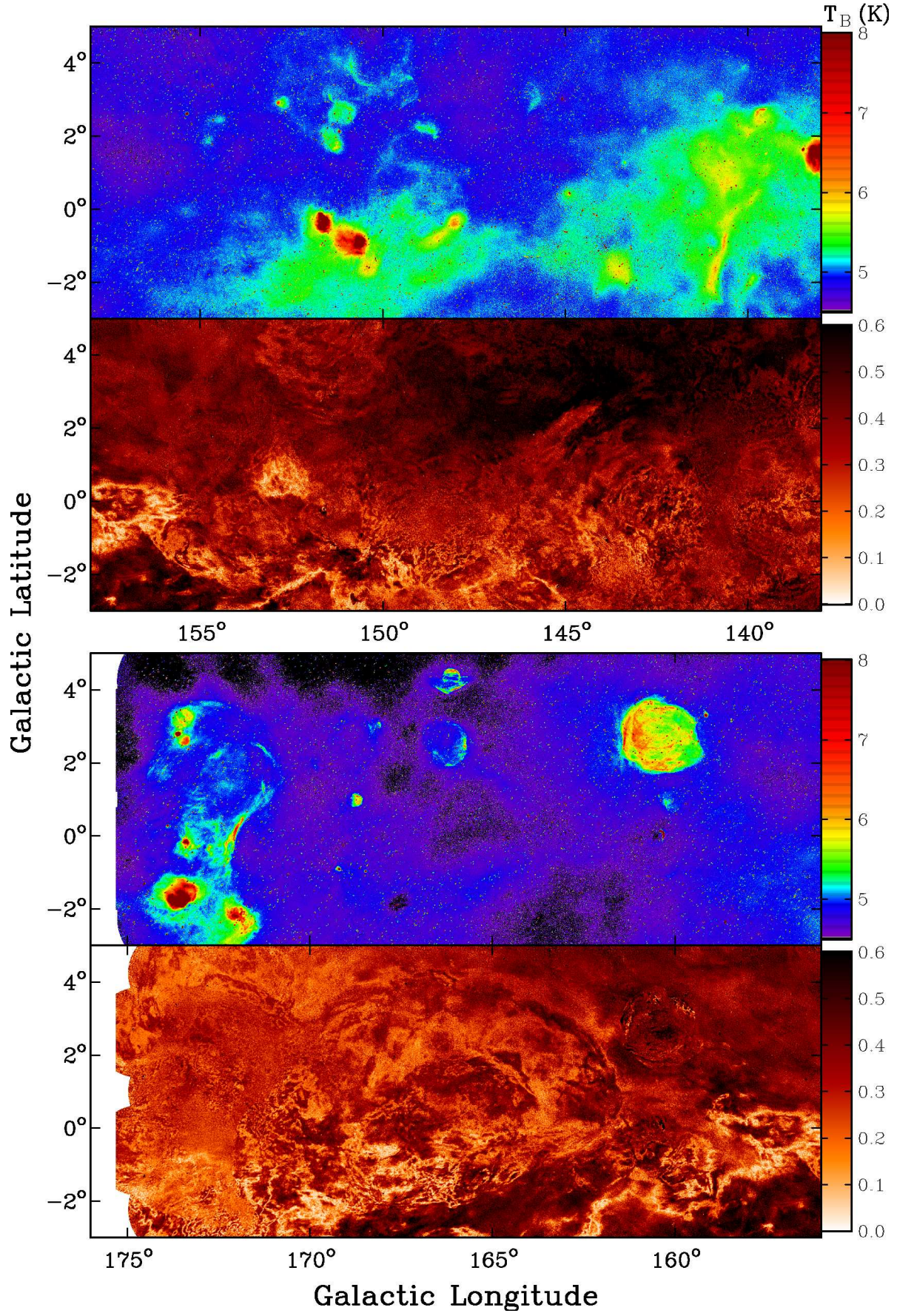
Fig. 5. Maps of total intensity (multi-colour) and polarized intensity (orange) in the regions $66° < \ell < 86°$ (top), and $84° < \ell < 104°$ (bottom).
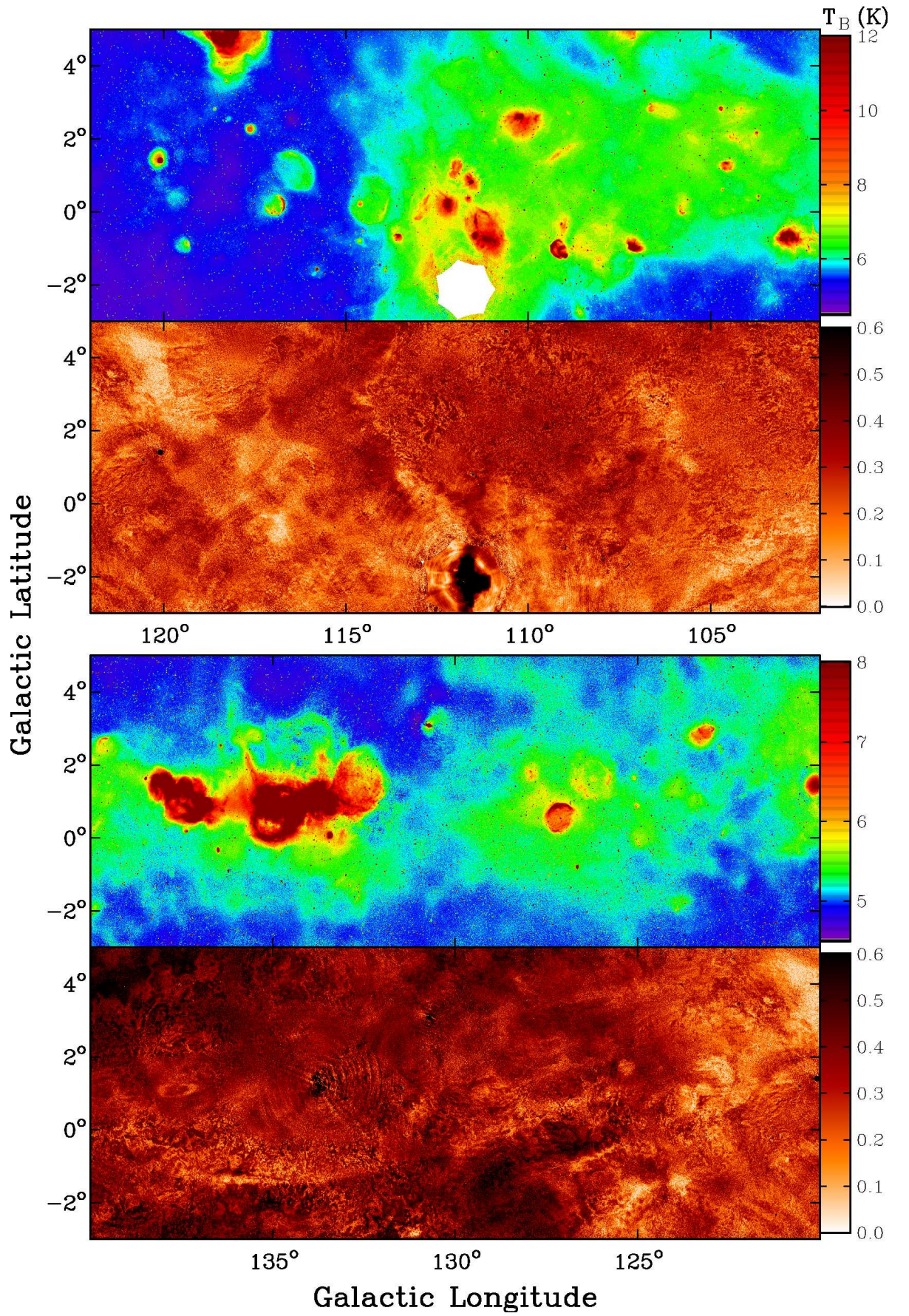
Fig. 6. Maps of total intensity (multi-colour) and polarized Intensity (orange) in the regions $102° < \ell < 122°$ (top), and $120° < \ell < 140°$ (bottom).

Fig. 7. Maps of total intensity (multi-colour) and polarized intensity (orange) in the regions $138° < \ell < 158°$ (top), and $156° < \ell < 176°$ (bottom).

and also easily detectable, while the signal in the total-intensity channel will be only 1 σ (if the H II region fills the beam).

Ironically, the very effect that makes ionized gas so easy to detect can be a drawback, because copious Faraday rotation produces depolarization. Depolarization is a reduction in observed fractional polarization that arises from vector averaging (Gray et al. 1999; Uyanıker et al. 2003). The averaging may occur (a) along the line of sight, in which case the phenomenon is known as *differential Faraday rotation* or *depth depolarization*, (b) within the telescope beam (*Faraday dispersion* or *beam depolarization*) or (c) within the receiver bandpass (*bandwidth depolarization*).

We see two kinds of depolarization features. The first kind is characterized by a sharp reduction of PI relative to the surroundings. This is depolarization by a relatively close H II region. Many of these H II regions can be recognized in total intensity or Hα images. The dense turbulent ionized material, probably accompanied by tangled magnetic field, strongly reduces the fractional polarization of emission from greater distances, and there is little synchrotron emission on the near side. The second kind is characterized by sharp boundaries within which the PI is still significant, but the structure becomes much smoother relative to the surroundings. In our data these instances are usually produced when a Local Arm H II region depolarizes more distant emission arising in the Perseus Arm. The relatively smooth polarized emission is synchrotron emission generated on the near side of the H II region, possibly affected by Faraday rotation. These effects can be used to estimate the distance to polarization features, based on known distances to H II regions (Kothes & Landecker 2004).

We note, however, that 4.9 GHz observations (Sun et al. 2007; Gao et al. 2010) show that some H II regions have quite different properties. At that frequency some faint H II regions generate significant regular Faraday rotation and must contain fairly strong regular fields. There is sufficient random fluctuation within these regions that they are depolarized at 1420 MHz. Detailed comparisons will be the subject of a future paper.

The concept of the *polarization horizon*, introduced by Uyanıker et al. (2003), is relevant in this discussion. The combined effects of depth depolarization and beam depolarization do not allow us to detect polarized emission beyond a certain distance. The distance to the polarization horizon depends on frequency, beamwidth, and direction. Kothes & Landecker (2004) show that, in the Cygnus direction, the distance to the polarization horizon is about 2 kpc: we are seeing predominantly local features between $\ell \approx 66°$ and $\ell \approx 100°$. At greater longitudes the images are a blend of local polarization features with those in the Perseus Arm. In general the local features are large and smooth, while the Perseus Arm features are characterized by small-scale structure that appears entirely random. Towards the anticentre the polarization horizon is well beyond the Perseus Arm, possibly even beyond the outer limits of the Galaxy.

8.4. Supernova remnants

Some SNRs appear as prominent polarized objects in the survey. The polarized signatures of CTB80 (G69.0+2.7), HB21 (G89.0+4.7), CTB104A (G93.7−0.2), Tycho's SNR (G120.1+0.4), 3C58 (G130.7+3.1), and HB9 (G160.9+2.6) are very clear. The emission from the direction of many SNRs is polarized but the polarized signal may not necessarily be SNR emission. First, careful subtraction of the local diffuse Galactic polarization is required to isolate any polarized emission from the SNR itself. Second, a polarized background may suffer

Faraday rotation within the SNR. Kothes et al. (2006) have made a thorough study of the 34 SNRs detected in the area of the data presented in this paper; they detected significant polarized emission from 18 of them. If the SNR is beyond the polarization horizon its polarized emission can not usually be detected (Uyanıker et al. 2003).

8.5. The Cygnus-X region

The Cygnus-X region, whose radio emission peaks at $\ell = 80°$, $b = 1°$, is the Local spiral arm seen end-on: in this direction many objects at distances 1 to 4 kpc lie close together on the sky (Wendker et al. 1991). Cygnus X is a strong emitter in total intensity, with an integrated flux density of about 1000 Jy at 1.4 GHz from a region roughly $6° \times 6°$ in size, and its emission is dominated by thermal emission (Wendker et al. 1991; Knödlseder 2000) although a few non-thermal sources are also present. Surprisingly, there is significant polarized emission roughly coincident with the total-intensity emission from Cygnus X, and the PI along the Galactic plane on either side of the emission complex (from $\ell \approx 70°$ to $\ell \approx 77°$ and from $\ell \approx 84°$ to $\ell \approx 91°$) is much lower (see Fig. 4 and Fig. 5). The same effect can be seen in all three datasets, the DRAO 26-m data, the Effelsberg data, and the DRAO Synthesis Telescope data: it occurs on all size scales.

At first sight it is puzzling that a thermal region can apparently produce polarized emission, but this can be interpreted by understanding the depolarization process. The ionized gas in Cygnus X is dense and turbulent, and, since we expect the frozen-in field to share these characteristics, Cygnus X will effectively scramble the polarization of any synchrotron emission that is generated behind it. The objects that comprise Cygnus X are concentrated between distances of 1 and 4 kpc. The polarized emission that is seen in Fig. 5 towards Cygnus X must therefore be generated and Faraday rotated along the nearest 1 kpc of the line of sight. On the other hand, along lines of sight to either side of Cygnus X there is no large concentration of depolarizing material, and emission generated along the entire line of sight is superimposed, and vector averaging over long paths leaves little polarized signal. This general direction is nearly aligned with the direction of the local magnetic field and we expect strong depth depolarization here.

The effect described can be exploited to study the local synchrotron emissivity (on this and on other lines-of-sight that intersect dense H II material). This is a topic beyond the scope of the present paper, but we note that a study over a range of wavelengths would be productive.

8.6. The HB3/W3/W4/W5 complex

The HB3/W3/W4/W5 complex ($\ell \approx 132°$ to $\ell \approx 139°$ at $b \approx 1°$) lies on the near side of the Perseus Arm at a distance of $\sim$2.2 kpc (Normandeau et al. 1996). Polarization features in the vicinity are well studied. Small-scale disorganized structure is depolarized by the H II regions W3, W4, and W5 (Gray et al. 1999) implying that it is generated by Faraday rotation in the Perseus Arm.

Gray et al. (1998) discuss a lens-shaped feature seen in Fig. 6 superimposed on W5 ($\ell = 137°.6, b = 1°.1$) and place it in the interarm at a distance of approximately 1 kpc. It is remarkable for its highly ordered structure in an area where all other polarization structure is disordered. From the Synthesis Telescope alone Gray et al. (1998) found ΔPA = 280° from edge to cen-

tre of this object requiring a change of RM of $\sim$110 rad m^{-2}. From the present data we find ΔPA = $\sim$25°, implying a much smaller ΔRM. This illustrates the problem inherent in interpreting aperture-synthesis data without the addition of single-antenna data. The general conclusions reached by Gray et al. (1999) about this object are unchanged by the smaller ΔPA from our new data but the distance constraints are somewhat loosened so that the object could be almost anywhere along the 2.2 kpc line of sight to W5.

With the wide spatial coverage of the images presented here we see a new "object" that may be related to HB3/W3/W4/W5, a large curved polarization feature that lies just south of the complex (Fig. 6). It is detectable from $\ell \approx 132°$ to $\ell \approx 140°$ at $b \approx -1°$. There is no doubt that this arc-like feature is real: it is detectable in the three individual data sets that have gone into making the survey images. Part of the arc is seen in the data presented by Gray et al. (1999), who commented that it might be related to W4. We refer to this feature as the W4 Polarization Arc. It shows many characteristics of a shock front. First, it is curved, and its curvature can be fitted approximately by a circle of radius $\sim$9°. Second, it has a steep outer edge (to larger radius) and a relatively shallow inner edge. If it is a shock, its polarization signature is the result of additional Faraday rotation in compressed material.

We have no information on its distance. It is either a feature of the local ISM or it is in the Perseus Arm. No association has yet been found with other ISM tracers that might allow us to discriminate between these two choices. For the sake of discussion, we will assume nominal distances for the two possibilities of 100 pc and 2.2 kpc, the latter value the distance to the W3/W4/W5 H ɪɪ regions (Normandeau et al. 1996).

The large angular extent and smooth structure of the Arc may favour a small distance. At a distance of 100 pc the length of the Arc would be about 25 pc. Shock fronts (*e.g.* SNRs) do not generally reach sizes much larger than this without severe distortion by ISM irregularities. If there is a complete spherical shock front its diameter would be about 30 pc. We would expect a local SNR of this size to have left detectable traces; their absence leads us to discount this interpretation.

If the Polarization Arc is a Perseus Arm feature at a distance of 2.2 kpc its size is $\sim$550 pc. While this is very large, there is evidence that may associate it with the W3/W4/W5 H ɪɪ complex. As explained above, the small-scale polarization structure which is seen around W4 is generated by Faraday rotation occurring in ionized gas near the H ɪɪ regions (Gray et al. 1999); the same may apply to the Arc. We note that the apparent centre of curvature of the Arc is at $\ell \approx 135°$, $b \approx 8°$, at virtually the same longitude as W4. The Arc may have been flattened by the density gradient below W4 (Normandeau et al. 1996), in which case the latitude of its centre is lower, within the W4 complex. We suggest that the W4 Polarization Arc may be at the same distance as the H ɪɪ complex, and it may be related to the star-formation activity there.

Normandeau et al. (1996) showed that the stars which ionize W4 (the star cluster OCl 352) have, through the influence of their winds, blown a large bubble above W4 (to positive Galactic latitudes). Although originally thought to be a Galactic "chimney" (a conduit for hot gas and ionizing radiation from the plane of the Galaxy into the halo), subsequent observations (Dennison et al. 1997; West et al. 2007) have shown the bubble is nearly closed about 325 pc above the plane. Reynolds et al. (2001) presented Hα data which reveal an ionized shell 1.3 kpc above W4. This ionized material, at the level where the Galactic disk blends into the halo, is probably a feature of an earlier phase of star formation in the same vicinity (discussed in West et al. 2007). The

Polarization Arc can be accommodated in a scenario where successive generations of star formation have made an impact over hundreds of parsecs of the ISM.

8.7. The planetary nebula Sharpless 2-216

The planetary nebula Sharpless 2-216 generates a polarization feature (at $\ell \approx 158°$, $b \approx 1°$) through Faraday rotation in its ionized shell (Ransom et al. 2008). Sh 2-216 is the closest planetary nebula, at a well-established distance of 129 pc. Its angular size of 1°7 translates to a physical diameter of 3.8 pc. The ionized shell, of density $\sim$10 cm^{-3}, generates a weak feature in total intensity but a strong Faraday rotation signature with $\Delta\psi \approx 60°$. Electron density in the shell can be deduced from optical and radio data, and path length is precisely known: the magnetic field can therefore be established. The line-of-sight field component is $\sim$5 μG, probably the interstellar field, slightly enhanced by compression in the planetary nebula shell. This is the first detection of magnetic field in a planetary nebula.

8.8. Stellar-wind bubble in the anticentre

A large arc in PI is evident at $162° < \ell < 169°$, $4° > b > 2°$ (see Fig. 7). Close examination shows that this is a circular structure, centred at $\ell = 166°$, $b = -1.0°$. A search of the CGPS database shows a clearly associated arc of H ɪ at $v_{lsr} = -17$ km s^{-1}; we refer to the object as GSH 166−01−17. This association places GSH 166−01−17 in the Perseus Arm at a distance of $\sim$1.9 kpc where its extent is some 350 pc.

The interpretation (Kothes et al., in preparation) sees GSH 166−01−17 as a superbubble blown by a cluster of stars over a period of 10 to 20 million years. A group of stars, ranging in type from B2 to B4, is still within the shell but there must have been stars of earlier type present to blow such a large bubble, and those stars have probably now exploded as supernovae, contributing to the internal energy of the bubble. There is (weak) evidence of non-thermal emission within the bubble, possibly the result of supernova explosions within the shell, and diffuse X-ray emission, presumably from hot interior material, can be seen in the ROSAT X-ray survey. Beyond these traces, the bubble sits in a remarkably empty part of the Galaxy. However, the bubble is surrounded by young objects, of typical age 1 million years, and it is conceivable that this is star formation triggered by the evolution of GSH 166−01−17.

A simple interpretation, based on the model of Weaver et al. (1977) can explain the polarization signature of the stellar-wind bubble. In the Weaver et al. model the centre of such a bubble is filled with very hot gas (temperature $\sim$10^6 K), of very low density, surrounded by a thick shell of shocked stellar-wind material at a temperature of $\sim$10^5 K. In GSH 166−01−17 there is apparently a toroidal magnetic field within this shell. Background polarized emission is Faraday rotated as it passes through the shell and adds vectorially to a polarized foreground. PI rises and falls, as seen in Fig. 7, as the rotated background and the foreground components reinforce and cancel. The toroidal field is presumably stellar in origin. If this interpretation is correct, GSH 166−01−17 is a prime example of stellar winds carrying magnetic energy from stars into the ISM.

Bubbles and superbubbles play a prominent role in current models of ISM evolution (de Avillez & Breitschwerdt 2005), and these objects are widely supposed to be affected by magnetic fields (Ferrière et al. 1991; Tomisaka 1998; Stil et al. 2009). Nevertheless, there are very few measurements of mag-
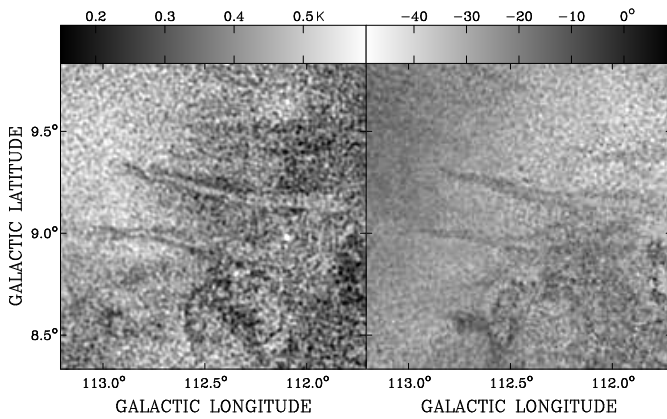
Fig. 11. The "fingers" at the interface between disk and halo regions. left panel shows polarized intensity and right panel polarization angle. See Section 8.9.

netic fields in such objects (for another example see West et al. 2007).

8.9. The high-latitude region

The high-latitude region, $101° \leq \ell \leq 116°$, $4°\!.5 \leq b \leq 16°\!.5$ is shown in Fig. 9. A rectangular boundary can be seen with edges at $\ell \approx 101°\!.5$ and $b \approx 14°\!.5$. Effelsberg data were not included outside these limits (to the upper and right hand edges of Fig. 9).

A striking feature of Fig. 9 is a transition from small-scale structure at lower latitudes to a much smoother structure above it. This transition is seen more clearly in Fig. 10 which shows PI only. The transition begins at $b \approx 8°$ and is complete across most of the longitude range shown by $b \approx 10°\!.5$. Below the transition the size of structures is about $3'$, but above it structure is distinctly smoother with scale size at least $20'$. The transition does not appear to be related to the change in PA that runs diagonally across Fig. 9 (seen as changing colour); that is probably a foreground effect. Such a transition in structure is suggestive of an interface between disk and halo regions. The very fact that we detect an abrupt transition implies that the boundary that we are seeing cannot be a feature of the Local Arm (we would not see a sharp transition from within the disk) – we must be seeing the "top" of the Perseus Arm, at a distance of ~3 kpc. At this distance the transition at $b \approx 10°$ is at a physical distance ~500 pc above the Galactic mid-plane. The characteristic sizes of $3'$ and $20'$ below and above the transition correspond to physical sizes of 3 pc and 17 pc respectively. The transition is reminiscent of the model of Kalberla & Kerp (1998) who envisage an abrupt transition between a turbulent disk and a smooth halo in which gas, cosmic rays and magnetic fields are in pressure equilibrium.

Figure 11 is enlarged to show one detail of the disk-halo interface. Three long "fingers" are seen in PI and PA, about $5'$ wide and $45'$ long. At a distance of 3 kpc they are ~480 pc above the mid-plane and their physical dimensions are 4 pc wide and 40 pc long. These fingers may be structures in magnetic field, structures in electron density, or some combination of the two. The change of ~20° that they produce in polarization angle implies a RM of about 7 rad m^{-2}. The fingers cannot be detected in available Hα images and there is no other information on electron density, so the magnetic field within them cannot be deduced. They are suggestive of some kind of magnetohydrodynamic instability at an interface between two fluids.

9. Conclusions, and extensions of this work

We have described techniques developed to make a survey of the polarized radio emission from the Galactic plane over a large area, combining data from aperture-synthesis and single-antenna telescopes to provide an accurate portrayal of emission features on all angular scales to the resolution limit of $\sim1'$. This survey represents a major advance in high-fidelity imaging of the polarized sky. We have presented data from the survey and have made preliminary interpretations of some features revealed by it.

Mapping the polarized sky opens a new "window" on the ISM because the appearance of the sky is dominated by Faraday rotation occurring along the propagation path through the Galaxy, to the point where the polarized sky does not resemble the total-intensity sky. Some general conclusions can be reached from this work that will be relevant to future polarization imaging.

– While Faraday rotation tends to break up large emission structures into smaller ones, there is still significant large-scale structure at 1.4 GHz. Consequently, interpretation of aperture-synthesis data will be severely limited unless single-antenna data are accurately incorporated into the images.

– Faraday rotation is a powerful tool for detecting ionized gas, and polarization observations will lead to the discovery of objects that cannot easily be detected by other means.

– There are features of the Galactic emission many degrees in extent; despite their large size they are very difficult to recognize without arcminute angular resolution.

– Polarization features trace structures in the magneto-ionic medium, in electron density or magnetic field or both, and observations of the diffuse polarized emission reveal a diversity of phenomena associated with this component of the ISM. The magneto-ionic medium is in part unstructured and very broadly distributed but it may also be associated with discrete objects such as SNRs, H ıı regions, planetary nebulae, and stellar-wind bubbles.

– Some of the features seen in polarization images are the products of propagation and depolarization effects of various kinds, and are not necessarily "objects" in the usual astronomical sense.
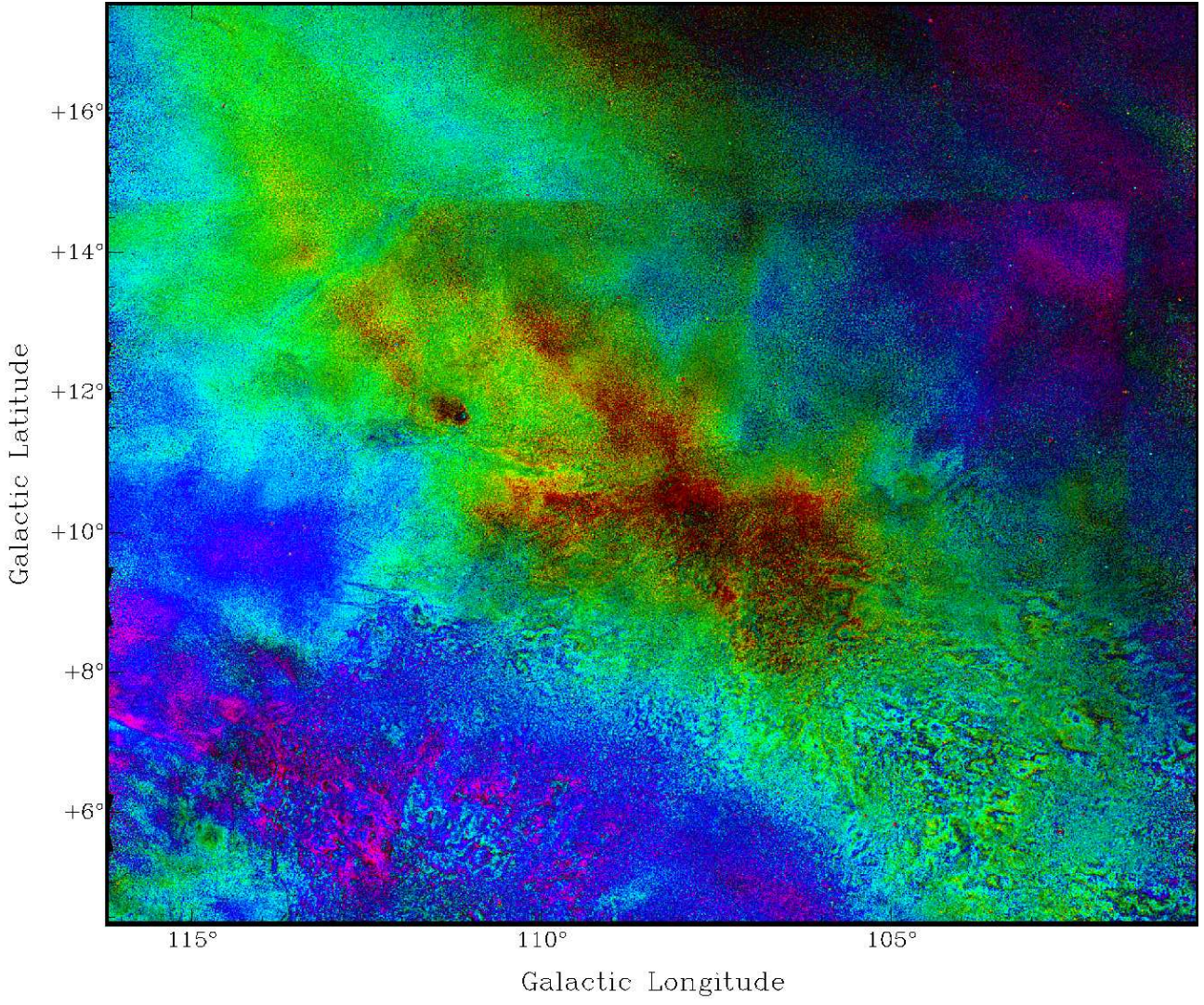
This survey has revealed a wealth of structure in the magneto-ionic medium on all scales. Future work on the data presented here will be directed at illuminating the relationship between these structures and other phases of the ISM. Information on other ISM tracers, particularly the CGPS datasets describing the atomic, ionized, and molecular gas and the dust, will be critical to the success of these studies.

The longitude range of the survey has been extended to $\ell \approx 55°$ towards the inner Galaxy and to $\ell \approx 195°$ beyond the anticentre. These new data will be processed using the techniques described in this paper.

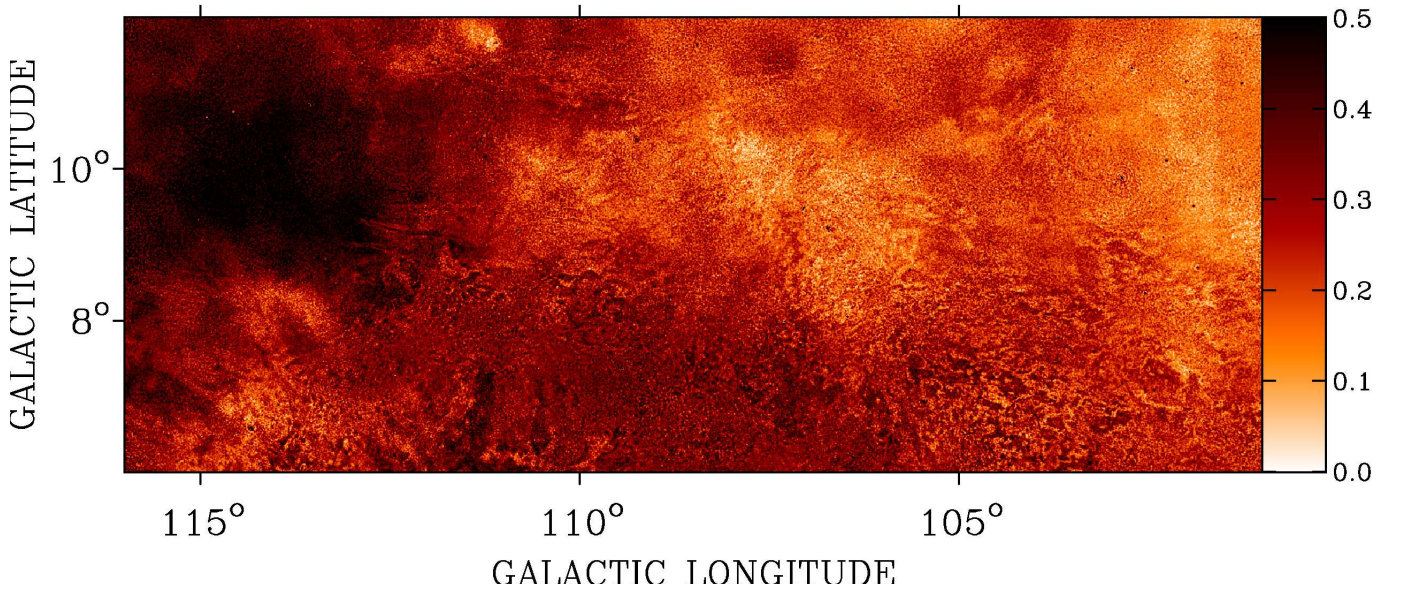**Fig. 9.** Polarization data in the high-latitude region. As in Fig. 4, intensity of colour depicts polarized intensity and hue depicts polarization angle. The range of polarized intensity is zero (dark) to 0.5 K (bright). The range of polarization angle is from −40° to +10°. Colour changes smoothly from red (PA≈−40°) through orange, yellow, green, blue, and purple, to red (PA≈+10°).

Fig. 10. Polarized intensity in the high-latitude region, showing a transition in structure between $b \approx 8°$ and $b \approx 10°.5$.

References

Baars, J. W. M., Genzel, R., Pauliny-Toth, I. I. K., & Witzel, A. 1977, A&A, 61, 99

Beck, R. 2001, Space Science Reviews, 99, 243

Brouw, W. N. & Spoelstra, T. A. T. 1976, A&AS, 26, 129

Brown, J. C. & Taylor, A. R. 2001, ApJ, 563, L31

Brown, J. C., Taylor, A. R., & Jackel, B. J. 2003, ApJS, 145, 213

Burn, B. J. 1966, MNRAS, 133, 67

Cao, Y., Terebey, S., Prince, T. A., & Beichman, C. A. 1997, ApJS, 111, 387

de Avillez, M. A. & Breitschwerdt, D. 2005, A&A, 436, 585

Dennison, B., Topasna, G. A., & Simonetti, J. H. 1997, ApJ, 474, L31

Duncan, A. R., Haynes, R. F., Jones, K. L., & Stewart, R. T. 1997, MNRAS, 291, 279

Duncan, A. R., Reich, P., Reich, W., & Fürst, E. 1999, A&A, 350, 447

Emerson, D. T. & Gräve, R. 1988, A&A, 190, 353

Ferrière, K. M., Mac Low, M.-M., & Zweibel, E. G. 1991, ApJ, 375, 239

Gaensler, B. M., Dickey, J. M., McClure-Griffiths, N. M., et al. 2001, ApJ, 549, 959

Gao, X. Y., Reich, W., Han, J. L., et al. 2010, A&A

Gray, A. D., Landecker, T. L., Dewdney, P. E., & Taylor, A. R. 1998, Nature, 393, 660

Gray, A. D., Landecker, T. L., Dewdney, P. E., et al. 1999, ApJ, 514, 221

Hachenberg, O., Grahl, B., & Wielebinski, R. 1973, IEEE Proceedings, 61, 1288

Haverkorn, M., Gaensler, B. M., McClure-Griffiths, N. M., Dickey, J. M., & Green, A. J. 2006, ApJS, 167, 230

Haverkorn, M., Katgert, P., & de Bruyn, A. G. 2000, A&A, 356, L13

Haverkorn, M., Katgert, P., & de Bruyn, A. G. 2003a, A&A, 403, 1045

Haverkorn, M., Katgert, P., & de Bruyn, A. G. 2003b, A&A, 403, 1031

Haverkorn, M., Katgert, P., & de Bruyn, A. G. 2003c, A&A, 404, 233

Heyer, M. H., Brunt, C., Snell, R. L., et al. 1998, ApJS, 115, 241

Hinshaw, G., Weiland, J. L., Hill, R. S., et al. 2009, ApJS, 180, 225

Junkes, N., Fürst, E., & Reich, W. 1987, A&AS, 69, 451

Kalberla, P. M. W. & Kerp, J. 1998, A&A, 339, 745

Kalberla, P. M. W., Mebold, U., & Reich, W. 1980, A&A, 82, 275

Kerton, C. R. & Martin, P. G. 2000, ApJS, 126, 85

Knödlseder, J. 2000, A&A, 360, 539

Kothes, R., Fedotov, K., Foster, T. J., & Uyanıker, B. 2006, A&A, 457, 1081

Kothes, R. & Landecker, T. L. 2004, in The Magnetized Interstellar Medium, Antalya, Turkey, ed. B. Uyanıker, W. Reich, & R. Wielebinski, 33–38

Landecker, T. L., Dewdney, P., Burgess, T. A., et al. 2000, A&AS, 145, 509

Ng, T., Landecker, T. L., Cazzolato, F., et al. 2005, Radio Science, 40, 5014

Normandeau, M., Taylor, A. R., & Dewdney, P. E. 1996, Nature, 380, 687

Noutsos, A. 2009, in IAU Symposium, Vol. 259, IAU Symposium, 15–24

Ott, M., Witzel, A., Quirrenbach, A., et al. 1994, A&A, 284, 331

Ransom, R. R., Uyanıker, B., Kothes, R., & Landecker, T. L. 2008, ApJ, 684, 1009

Reich, P. & Reich, W. 1986, A&AS, 63, 205

Reich, W. 1982, A&AS, 48, 219

Reich, W. 2006, in Cosmic Polarization, ed. R. Fabbri, 91–130

Reich, W., Fürst, E., Reich, P., et al. 2004, in The Magnetized Interstellar Medium, Antalya, Turkey, ed. B. Uyanıker, W. Reich, & R. Wielebinski, 45–50

Reich, W., Reich, P., & Fürst, E. 1990, A&AS, 83, 539

Reid, R. I., Gray, A. D., Landecker, T. L., & Willis, A. G. 2008, Radio Science, 43, 2008

Reynolds, R. J., Sterling, N. C., & Haffner, L. M. 2001, ApJ, 558, L101

Smegal, R. J., Landecker, T. L., Vaneldik, J. F., Routledge, D., & Dewdney, P. E. 1997, Radio Science, 32, 643

Sofue, Y. & Reich, W. 1979, A&AS, 38, 251

Sokoloff, D. D., Bykov, A. A., Shukurov, A., et al. 1998, MNRAS, 299, 189

Steer, D. G., Dewdney, P. E., & Ito, M. R. 1984, A&A, 137, 159

Stil, J., Wityk, N., Ouyed, R., & Taylor, A. R. 2009, ApJ, 701, 330

Sun, X. H., Han, J. L., Reich, W., et al. 2007, A&A, 469, 1003

Sun, X. H., Reich, W., Waelkens, A., & Enßlin, T. A. 2008, A&A, 477, 573

Taylor, A. R., Gibson, S. J., Peracaula, M., et al. 2003, AJ, 125, 3145

Tomisaka, K. 1998, MNRAS, 298, 797

Uyanıker, B., Fürst, E., Reich, W., Reich, P., & Wielebinski, R. 1998, A&AS, 132, 401

Uyanıker, B., Fürst, E., Reich, W., Reich, P., & Wielebinski, R. 1999, A&AS, 138, 31

Uyanıker, B. & Landecker, T. L. 2002, ApJ, 575, 225

Uyanıker, B., Landecker, T. L., Gray, A. D., & Kothes, R. 2003, ApJ, 585, 785

Weaver, R., McCray, R., Castor, J., Shapiro, P., & Moore, R. 1977, ApJ, 218, 377

Wendker, H. J., Higgs, L. A., & Landecker, T. L. 1991, A&A, 241, 551

West, J. L., English, J., Normandeau, M., & Landecker, T. L. 2007, ApJ, 656, 914

Westerhout, G., Seeger, C. L., Brouw, W. N., & Tinbergen, J. 1962, Bull. Astron. Inst. Netherlands, 16, 187

Wielebinski, R., Shakeshaft, J. R., & Pauliny-Toth, I. I. K. 1962, The Observatory, 82, 158

Wieringa, M. H., de Bruyn, A. G., Jansen, D., Brouw, W. N., & Katgert, P. 1993, A&A, 268, 215

Willis, A. G. 1999, A&AS, 136, 603

Wolleben, M. 2007, ApJ, 664, 349

Wolleben, M., Landecker, T. L., Hovey, G. J., et al. 2010, AJ, 139, 1681

Wolleben, M., Landecker, T. L., Reich, W., & Wielebinski, R. 2006, A&A, 448, 411